JOURNAL OF MATERIALS SCIENCE **35** (2000) 4907–4912

Electronic properties of Sb_xSe_{1-x} glasses

V. I. MIKLA*, I. P. MIKHALKO, YU. YU. NAGY, A. V. MATELESHKO, V. V. MIKLA
Institute for Solid State Physics and Chemistry, Uzhgorod State University, Voloshina Str. 54, 294000 Uzhgorod, Ukraine
E-mail: mikla@iss.univ.uzhgorod.ua

The mechanism of incorporation of metallic antimony in amorphous and glassy samples of the Sb_xSe_{1-x} ($0 \leq x \leq 0.10$) system is studied by measuring the xerographic discharge characteristic, drift mobility and optical absorption. It is observed that the addition of antimony increases the DC conductivity, decreases the electron mobility, changes the xerographic parameters and decreases the optical gap of the system. The Compositional dependence of the electronic properties are related to the defect states produced due to incorporation of Sb atoms in glassy selenium matrix.

1. Introduction

The physical properties of chalcogenide glasses which are arsenic free have attracted much interest for physical and technical reasons. Among these non-crystalline materials, the Sb_xSe_{1-x} glasses are attractive candidates for applications requiring low melting temperatures, low thermal conductance and high viscosity. In particular, thin films of the Sb-Se system, which can undergo an amorphous-crystalline phase transition, were studied as reversible optical recording candidates [1].

The amount of metallic antimony in Sb-Se can appreciably affect the optical and electrical transport properties. These properties are affected mainly by the localized gap states. Some of the basic properties of amorphous thin films from the Sb-Se system have been studied by Wood *et al.* [2]. However, the electronic properties of the Sb_xSe_{1-x} glasses have not been understood fully. For instance, little insight into the mobility gap structure has been obtained.

This paper attempts to collect and discuss our recent results on electronic properties for Se-rich Sb_xSe_{1-x} alloys.

2. Experimental

Samples investigated were melt-quenched bulk glasses and amorphous films from the system Sb_xSe_{1-x} ($0 \leq x \leq 0.10$). Glasses were melted in 1.2 cm outside diameter, 1.0 cm internal diameter quartz tubes of about 15 cm length. Proper quantities of the high-purity elements (99.999%) were sealed in evacuated quartz ampoules and heated in a suitable furnace up to 800°C for at least 24 hours. The melt was continuously rotated to ensure homogenization and was quenched in ice cold water. Differential thermal analysis, electron microscopy and Raman spectroscopy confirmed the glassy nature of the alloys and the absence of phase separation, etc. The glass so obtained was further used for the evaporation of amorphous films.

Amorphous films of Sb_xSe_{1-x} were deposited onto aluminum substrates by vacuum thermal evaporation in a standard coating unit at a pressure of 10^{-3} Pa. The substrates were maintained at 25°C (below the glass transition temperature of Se) during evaporation. Sample thicknesses were typically ~20 μm. After fabrication, the films were aged in the dark for about two months at ~25°C (natural aging) for their physical properties to stabilize. During the aging process, the structure relaxes towards its metastable equilibrium-like state while the structure dependent properties, e.g. concentration of defects which control the electronic properties, equilibrate. X-ray diffraction studies and Raman scattering measurements showed no evidence of crystallinity in the samples prepared by the method used.

The optical transmission spectra were measured by a double-beam spectrophotometer (CSC 21 model) in the region 200–2500 nm and the transmittance was used to calculate the absorption coefficient.

Xerographic techniques, initially developed to characterize electrophotographic receptors, are widely applicable to the study of amorphous thin films and photoconductive insulator thin films [3–6]. Such a xerographic potential probe technique is one of the unique means to characterize electronic gap states which play a key role in influencing (photo)electronic properties. The electrophotographic properties of the Sb_xSe_{1-x} samples were measured using the conventional xerographic technique. The instrument used for the measurements consisted of a corotron, a sample rotating mechanism, a light exposure mechanism and a surface potential measuring apparatus. Following the initial charging process, the sample was exposed to strongly absorbed 450 nm step illumination from a tungsten light source during which time the decay of the surface electrostatic potential was monitored by the electrostatic voltmeter. The surface potential decays to a potential V_r (termed the residual potential) and the resulting photo-induced discharge curve can be used to determine the

* Author to whom all correspondence should be addressed.

xerographic photosensitivity of the sample. The xerographic step could be repeated any number of times to obtain a cycled-up residual surface potential V_{rn} as a function of the xerographic cycle n.

Time-of-flight (TOF) transient photoconductivity measurements were used to study the characteristics of the charge carrier transport in Sb_xSe_{1-x} alloys. The measurement technique was similar to that developed by Spear [7]; the details of the TOF apparatus have been described previously [4, 8–10]. A semi-transparent Au electrode was sputtered on the top surface of the film to complete a sandwich structure: $Al/(Sb_xSe_{1-x})/Au$. In the present case we have used a nitrogen gas laser ($\lambda = 337$ nm) to photoexcite the carriers. The output light pulse width was ~8 ns. All experiments were essentially single shot type measurements in which the sample was pulsed from the laser and the corresponding photocurrent was captured on a single event storage oscilloscope. To preclude possible thickness variations of the sandwich structure causing the resulting dispersion, different regions of the Au contact were illuminated and the resulting photocurrent waveforms compared. Between measurements, the sample was short-circuited and rested in the dark to discharge any trapped charge.

3. Results and discussion

3.1. The basic properties

First, we begin with a brief review of some fundamental physical properties. Fig. 1 shows the dependence of the glass transition temperature, Tg, on the composition of the Sb-Se glasses. We defined the glass transition temperature in the usual way, as the midpoint of the transition endotherm. Starting with 1 at.% Sb, our data for Tg show a monotonic increase with increasing Sb concentration. At the same time, we observe a change of slope (step-like behavior) between $x = 0$ and $x = 0.02$ signaling a change in the structure. For each composition we carried out several experiments and all showed good reproducibility. Note that the experimental points represent average values with the size of the plotted bars comparable with the size of the plotted experimental point. It should be noticed further that microhardness and density show similar compositional trends with a local rise around the same composition.

For all Sb-Se compositions used in this study, the dark dc conductivity can be expressed in the temperature range considered by an Arrhenius-type relation

$$\sigma = \sigma_0 \exp\left(\frac{-E_\sigma}{kT}\right) \tag{1}$$

where E_σ is the activation energy and σ_0 is the conductivity pre-exponential factor. The activation energy and the conductivity at 300 K are presented in Table I. It can be seen that both the conductivity and the activation energy decrease with increasing Sb content.

The absorption coefficient α determined from transmission measurements is shown in Fig. 2 as a function of photon energy, $h\nu$. As seen in the figure, in the glassy system Sb-Se the optical absorption edge (the Urbach tail region) shifted to longer wavelengths and the slope became smaller as the percentage of Sb increased. This is a general trend over most of the composition range. Absorption above the fundamental edge follows the familiar Tauc law [11], that is

$$\alpha h\nu = C(h\nu - E_T)^2, \tag{2}$$

TABLE I The dc conductivity (300 K), the corresponding activation energy and the Tauc gap of Sb_xSe_{1-x} glasses

Sb content (at.%)	σ_{ROOM} (Ω^{-1} cm^{-1})	E_σ (eV)	dV/dt (V s^{-1})	$t_{v_0}/2$ (s)	E_0 (eV)
0	*1×10^{-14}	1.05	7.8×10^{-2}	267	2.04
2	*1×10^{-13}	1.02	2.0×10^{-1}	81	2.02
5	8×10^{-11}	0.90	1.83	76	
8	9×10^{-10}	0.84			
10	4×10^{-10}	0.76			1.85
20	1×10^{-9}	0.72			1.62
40	2×10^{-8}	0.62			1.50

*Data with $\sigma < 10^{-11}$ Ω^{-1} cm^{-1} refer to the sandwich geometry.

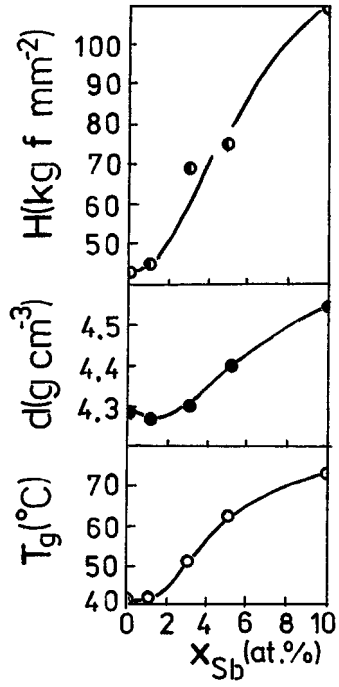

Figure 1 Dependence of the glass transition temperature T_g, density d, and microhardness H on the composition of the Sb-Se glass system.

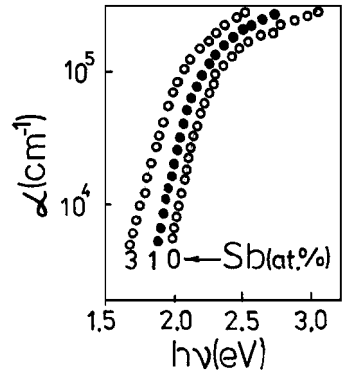

Figure 2 Optical absorption coefficient as a function of energy for different Sb_xSe_{1-x} alloys.

where $h\nu$ is a photon energy, E_T is the Tauc gap and C is a constant indicating how steeply the absorption rises with energy. For most compositions, there was no deviation from the square law at the highest absorption value measured in this study; exceptions being Se and films with less than 1 at.% Sb. The latter follow a linear law

$$\alpha h\nu = C_1(h\nu - E_1) \tag{3}$$

in the range 2.1–2.5 eV. Here C_1 is a constant and E_1 is an extrapolated optical gap. The addition of less than 1 at.% Sb to pure Se was enough to cause a complete transition from the anomalous linear behaviour of Equation 3 to Tauc's law. The room-temperature values of E_T (averaged over several samples) for various Sb_xSe_{1-x} compositions are given in Table I. It should be noted that the Tauc gap E_T is close to that of pure Se for small Sb concentrations (<1 at.% Sb) and then it decreases almost linearly (up to nearly 40 at.% Sb) as x increases.

3.2. Thermal generation of mobile carrier

Typical dark discharge characteristics (which include the rate dV/dt of decay and the time $t_{V_0}/2$ required the surface potential to decay to half of its original value $V_0/2$) for pure Se and Se containing small amounts of antimony are presented in Table I. It is apparent that for pure a-Se the decay of the surface potential is relatively slow. Comparison of the respective characteristics for a-Sb_xSe_{1-x} with the dark discharge behaviour of pure a-Se shows clearly that alloying a-Se with antimony increases the dark decay rate. As can be seen from the plots of the time derivative dV/dt against t, the discharge rates in a-Sb_xSe_{1-x} are not constant but decrease with time (Fig. 3).

One can expect the following possible physical mechanisms to cause the dark discharge [4, 12, 13]:

(a) surface generation and injection of trapped electrons and their consequent transport across the sample,
(b) substrate injection,

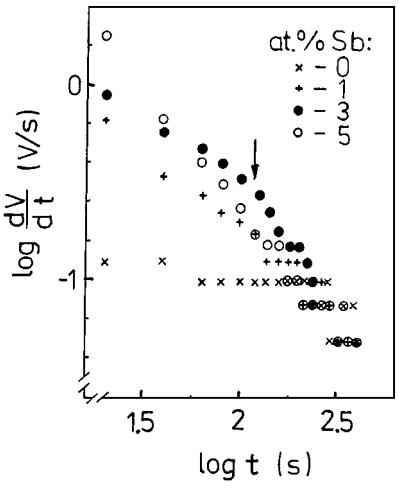

Figure 3 Typical discharge rate data for Sb_xSe_{1-x} films of indicated Sb content.

(c) bulk thermal generation of carriers of one sign and depletion.

With relatively thick films ($L = 10$–$50\ \mu$m) and a good blocking contact between a-Se-based films and the preoxidized A1 substrate the latter phenomenon dominates.

Xerographic dark discharge experiments on Sb_xSe_{1-x} glassy alloys indicated that the decay of the surface potential over the time scale of the experiment was controlled by the depletion discharge process. In general, the xerographic depletion discharge model is based on bulk thermal generation involving the ionization of a deep mobility gap center to produce a mobile charge carrier of the same sign as the surface charge and an oppositely charged ionic center [12, 13]. Assuming negative charging, a mobile electron would be thermally generated and the ionized center would be positive. As thermally generated holes are swept out by the electric field, a positive bulk space charge builds up with time in the specimen, causing the surface potential to decay with time.

Fig. 3 depicts typical dark discharge data for different compositions, which illustrate the predicted characteristics of depletion discharge behavior. Inflections in the log-log plots at the respective depletion times (marked by arrow for the case of $Sb_{0.03}Se_{0.97}$ composition) are readily identifiable. From the temperature dependence of depletion time it is estimated that the emitting sites are located $\sim 0.9 \pm 0.05$ eV below the conduction band mobility edge. Some special problems can, however, complicate the observation of a depletion kink in pure a-Se. The dark discharge rate was typically so slow in a-Se that results were always perturbed by injection. The central reason for pure Se possessing good dark decay characteristics is (a) the remarkably small integrated number of deep localized states ($\sim 10^{13}$ cm^{-3}) in the mobility gap of a-Se, and (b) the energy location of these states is deep ($E_t \sim 1.0$ eV) in the mobility gap, so that the thermal generation process of carriers from these centers is slow [4, 13, 14].

It is found that in a-Sb_xSe_{1-x} alloys, electrons (the mobile carrier species) are depleted (n-type system) during dark decay leaving behind deeply trapped positive space charge. Note that the same situation prevails in alkali-doped a-Se [15].

3.3. Photoinjected carrier transport

Both the electron and hole drift mobilities can be measured in pure amorphous selenium by the TOF technique, and at temperatures above 200 K, a well-defined transit pulse is observed. Fig. 4 shows a typical TOF electron and hole signal of a space charge free a-Se. We see that the transient profile for a well-relaxed (dark-adapted) sample is a quasi-rectangular pulse. The photocurrent remains approximately constant up to 0.2 and 6 μs (for holes and electrons respectively), then decreases abruptly. The signals indicate essentially nondispersive transport. The transit time t_T was defined to correspond to the break point in the photocurrent. This represents the transit time of the

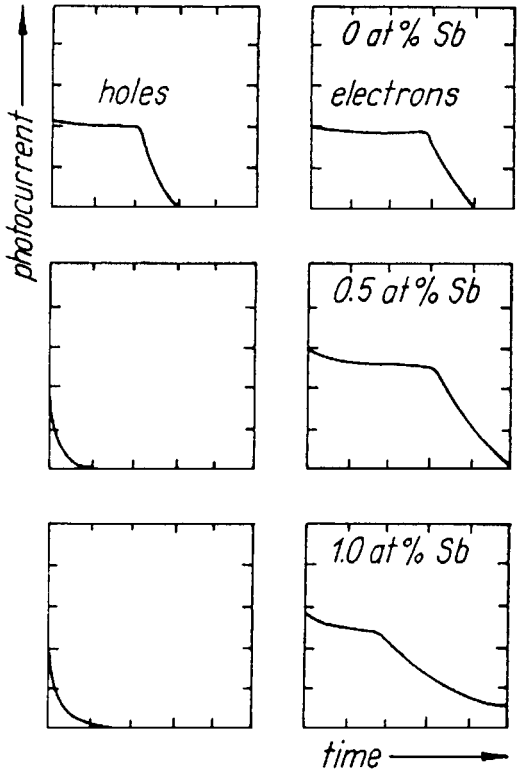

Figure 4 Oscilloscope traces of typical TOF transient current waveforms in amorphous selenium alloyed with Sb. For Se, $E = 8.0 \times 10^6$ V m^{-1} and 0.1 μs per division for holes and 2 μs per division for electrons. For 0.5 at.% Sb, $E = 9.0 \times 10^6$ V m^{-1} and 0.1 μs per division for holes and 2 μs per division for electrons. For 1 at.% Sb, $E = 8.8 \times 10^6$ V m^{-1} and 0.1 μs per division for holes and 5 μs per division for electrons.

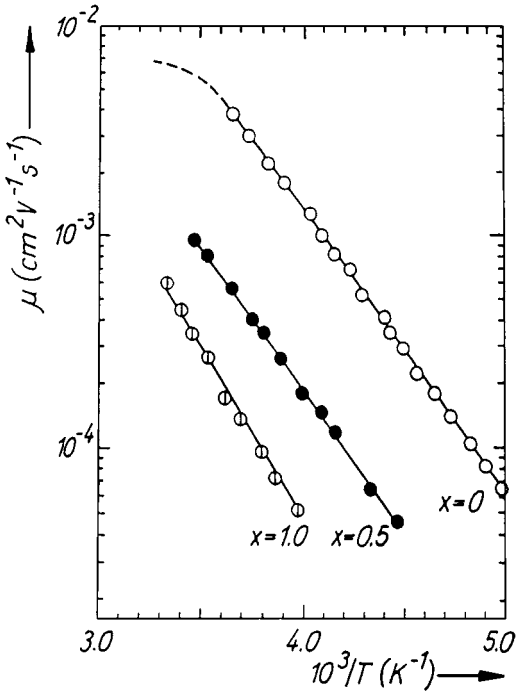

Figure 5 Temperature dependence of electron drift mobility in amorphous Sb_xSe_{1-x}. The respective values of x (in units of at.%) are indicated in the figure.

fastest carriers. The mobility, μ, is then calculated using $\mu = L^2/(t_T V_0)$ where V_0 is the applied voltage and L is the sample thickness. These room termperature values of the drift mobility, $\mu^h \approx 2 \times 10^{-1}$ cm^2 V^{-1} s^{-1} and $\mu^e \approx 7 \times 10^{-3}$ cm^2 V^{-1} s^{-1}, are in remarkably good agreement with reported values [4, 8, 14, 16, 17]. The effect of Sb addition to a-Se on the room temperature transit pulse shapes is summarized in Fig. 4. Note that for a-Sb_xSe_{1-x} films it was not possible to detect any pulses associated with the transit of hold carriers. In all samples, the hole response showed a rapid decay with no apparent break. There are two plausible explanations. First, the signal is limited by the presence of deep gap states with extremely high efficiency for carrier trapping. Second, it might be argued that alloying may have increased the conductivity of the samples so that TOF experiments are no longer applicable. However, results showed that although the conductivity increases with Sb addition, it remains sufficiently low ($\leq 10^{-11} \Omega^{-1}$ cm^{-1}) for TOF experiments to be applicable. It is interesting that the hole response in As-alloyed a-Se has also been found to be undetectable in the range 2–4 at.% As [16, 18].

The effect of Sb on electron transport is not so drastic. Although Sb alloying increases the transit time dispersion, the transit time shown contains a clearly identifiably break in the wave form. The electron drift mobility in a-Sb_xSe_{1-x} alloys exhibits Arrhenius behaviour (Fig. 5). The experimentally observed activation energy of a-Se, namely $E_\mu \approx 0.33 \pm 0.01$ eV, remains almost insensitive to Sb addition. At the same time, the mobility decreases with increasing Sb content. It is reasonable, within the framework of a shallow-trap-controlled mobility model [19], to interpret our TOF observations in the following manner. In pure Se, electron transport is controlled by a narrow manifold of traps located about 0.33 eV from the conduction band mobility edge. The addition of Sb to Se, as we believe, broadens the distribution of shallow traps, thus increasing the relative dispersion of photocurrent transients (see Fig. 3). The decrease in electron mobility with increasing Sb content can be accounted for by the increase in the density of shallow traps with E_μ remaining constant at approximately 0.33 eV.

3.4. Xerographic photosensitivity

In essence, the xerographic photosensitivity (S) of a photoreceptor material determines the rate of decay, dV/dt, of the electrostatic surface potential of the samples during a photoinduced discharge. The xerographic photosensitivity definition adopted here is simply based on the amount of light energy required for the surface potential to decay to half of its original value ($V_0/2$) during photoinduced discharge (i.e. the fractional change in the surface potential per unit light exposure).

Fig. 6 shows a dark decay curve and a photoinduced discharge curve for the a-$Sb_{0.03}Se_{0.97}$ film. It can be seen that the sample exhibits relatively little dark decay. Nevertheless, in order to take into account the surface charge reduction during illumination and to evaluate S accurately, the contribution of the dark discharge to the total change in the surface potential during PID was subtracted ($V_0 - V_d$ in Fig. 6).

The xerographic spectral response for both a-$Sb_{0.03}$ $Se_{0.97}$ and pure Se are shown in Fig. 7. It is apparent

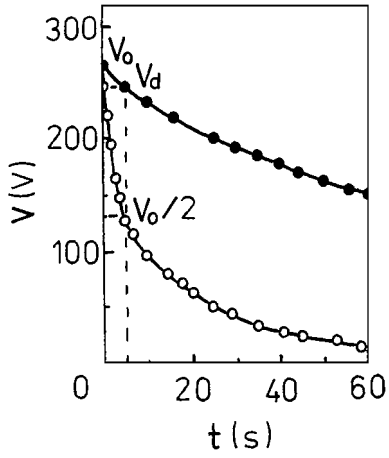

Figure 6 Dark decay curve (solid circles) and photoinduced discharge curve (open circles) for $Sb_{0.03}Se_{0.97}$.

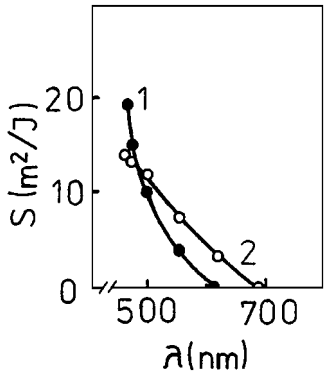

Figure 7 Xerographic photosensitivity (S) versus exposure wavelength (λ) for pure Se (1) and $Sb_{0.03}Se_{0.97}$ (2) alloy films. For all measurements, the light intensity (I) was kept constant at 0.7 J m^{-2} s^{-1} and the electric field was kept at $E = 2.3 \times 10^5$ V cm^{-1}. Note that the experimental points represent average values with typical error bars comparable with the size of the plotted experimental point.

that as Sb is added to a-Se, the photosensitivity at a particular wavelength increases. More precisely this means that the xerographic photosensitivity for Sb_xSe_{1-x} alloy is somewhat greater at longer wavelengths ($\lambda > 670$ nm) than for pure Se, and smaller at shorter wavelengths ($\lambda < 500$ nm). Note that other compositions of Sb-Se alloy showed similar trends. The result of increased xerographic photosensitivity of the Sb-Se alloys at longer wavelengths suggests that the addition of antimony to a-Se causes a reduction of the band gap of the material. It should be noticed here that the xerographic photosensitivity depends not only on the absorption coefficient, α, but also on the quantum efficiency, η, for generating mobile charge carriers as well as the transport properties (the $\mu\tau$ product) [4].

For the films under examination the residual voltage V_r (a measurable surface potential at the end of the illumination) increases with Sb content (Fig. 8). The residual potential is due to trapped electrons in the bulk of the specimen. The simplest theoretical model which is based on range limitation and weak trapping ($V_r \ll V_0$) relates V_r to $\mu\tau$ (the drift mobility, μ, and lifetime, τ, product) via the Warter equation [20]:

$$V_r = \frac{L^2}{2\mu\tau} \tag{4}$$

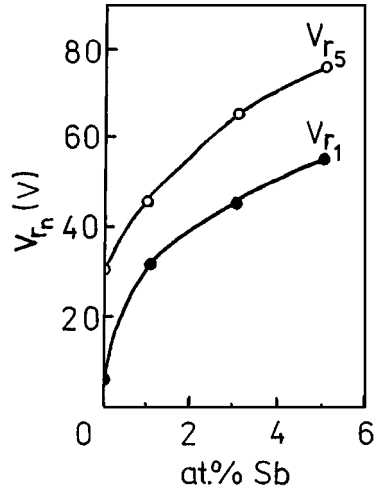

Figure 8 Effect of antimony on the residual potential (measured after 1st and 5th cycles) of Sb-Se alloy. Typical error bars are comparable with the size of the experimental point.

where L is the sample thickness. For example, addition of 3 at.% Sb leads to a change in the first cycle residual voltage from 4 to 44 V which is equivalent to a change of the carrier range, $\mu\tau$, from 10^{-7} to 10^{-6} cm^2/V. Substituting $\mu^e \sim 7 \times 10^{-3}$ $cm^2/(V\,s)$ for pure Se and $\mu^e \sim 6 \times 10^{-4}$ $cm^2/(V\,s)$ for $Sb_{0.03}Se_{0.97}$ into the corresponding equation we find carrier lifetimes $\tau \approx 2 \times 10^{-4}$ s and $\tau \approx 1.3 \times 10^{-3}$ s in a-Se and a-$Sb_{0.03}Se_{0.97}$. It is necessary to note here that in general, bulk deep trapping lifetimes computed from the first cycle residuals are in agreement with lifetimes measured in the time-of-flight mode under range-limited conditions.

Fig. 9 displays the buildup of the residual voltage V_{rn} on an a-$Sb_{0.03}Se_{0.97}$ film with the number of xerographic cycles n. The rate of increase in V_{rn} with n decreases as cycling increases, until eventually for large n (≥ 6 in our case) V_{rn} tends to a saturation value V_{rs}. As described earlier [21], the saturation residual potential provides an experimental measure of the integrated number of deep traps (trap-release rates are much slower than those from shallow traps which control drift mobility). V_{rs} is then simply given by

$$V_{rs} = \frac{eN_tL^2}{2\varepsilon} \tag{5}$$

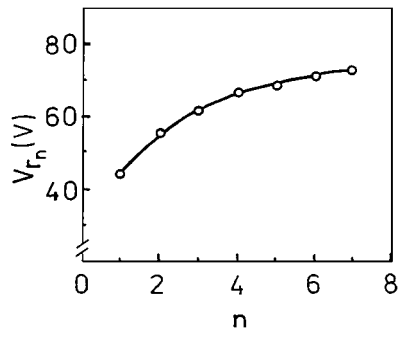

Figure 9 The build-up in the residual voltage with number of xerographic cycles in a-$Sb_{0.03}Se_{0.97}$ filmes. One charge-discharge cycle consists of 60 s light decay with a 1000 l× tungsten lamp after corona charging. The typical standard deviation is comparable with the size of the experimental point.

where N_t is the deep-trap concentration and ε is the dielectric constant. Both the first residual and the cycled-up saturated residual potential are sensitive to alloying. For example, when pure amorphous Se films are alloyed with antimony, the buildup of the residual potential occurs more rapidly toward a much higher saturated residual potential. We obtain, for instance, $N_t \sim 2\times 10^{14}$ cm^{-3} and $N_t \sim 10^{15}$ cm^{-3} for a-Se and $Sb_{0.03}Se_{0.97}$, respectively.

The above photoelectric properties of a-Sb_xSe_{1-x} alloys can be at least qualitatively explained by using concepts based on charged structural defects, called valence alternation pairs (VAP) or intimate valence alternation pairs (IVAP). These correspond to some of the chalcogen atoms being under- and overcoordinated [22]. It seems reasonable that dark discharge and residual voltage build-up involve essentially the same species of localized centers. Further, it is also possible that we may be observing amphoteric behaviour by IVAPs. For pure Se, an IVAP comprises over- and undercoordinated selenium atoms Se_3^+ and Se_1^- in close proximity. An IVAP center would be seen as a "neutral trap" by the carrier. The capture of an electron by Se_3^+ exposes the negative charge on Se_1^- and explains the residual voltage detected. At the same time, the emission of an electron from the Se_1^- uncovers the positive charge on Se_3^+ which causes the dark decay. Although the question remains whether the neutral center is a D^0 type defect or whether it is an IVAP defect, the measured radius of 3 Å in [23] is representative of an IVAP capture radius.

There are a number of desirable electrical characteristics that a useful photoreceptor should exhibit. Our experimental results show that dark decay rate, residual voltage and drift mobility are all sensitive to antimony. Carrier drift mobility decreases with antimony whereas dark decay rate and residual voltage increase. All these effects are undesirable in xerography. At the same time, the main advantage of a-Sb_xSe_{1-x} is that its spectral response can be readily shifted to longer wavelengths by increasing the Sb content, which allows for photoreceptor designs that can respond to a variety of illumination spectra. In addition, it may be possible to improve the charge transport parameters by halogen doping. Indeed, $C1$ is known to compensate for As (same group as Sb) induced deep traps in a-Se [24]. By using a double-layer photoreceptor consisting of a thin a-Sb_xSe_{1-x} layer for photogeneration and a thick a-Se layer for charge transport, the xerographic parameters can be further improved. It is interesting to consider the above results in relation to other Se-based binary alloys. As we have shown, in the range of compositions investigated, many properties (physico-chemical, optical, electronic) of the Sb_xSe_{1-x} system change around $x = 0.01$–0.02. The same behaviour is observed [25] for the As_xSe_{1-x} system, which has extrema (non-monotonicity) in several properties near the composition $x \approx 0.04$. A possible explanation suggested in [25] is that the above peculiarities are associated with the topological threshold which occurs when the chainring-like structure changes to a chain-like structure. This explanation can be extended for the case of Sb_xSe_{1-x} alloys, however more additional experimental data are needed for such suggestion.

4. Summary and conclusions

The mobile carrier Species controlling the xerographic depletion discharge in a-Sb-Se alloys are electrons. Thermal generation of free electrons in a-Sb_xSe_{1-x} is accompanied by the simultaneous formation of deeply trapped positive space charge. We find that antimony alloying progressively enhances the free electron thermal generation rate relative to the pure specimen.

As is apparent from the large xerographic residual potentials for Sb_xSe_{1-x} alloys, the addition of Sb to a-Se seems to greatly increase the concentration of deep localized states within the mobility gap of the material.

The results indicate that in the long wavelength region (e.g. $\lambda \sim 600$ nm) the photosensitivity for the a-Sb_xSe_{1-x} films is higher than for the pure selenium probably due to a greater quantum efficiency.

References

1. F. V. PIROGOV, *J. Non-Cryst. Solids* **114** (1989) 76.
2. C. WOOD, R. MUELLER and L. R. GILBERT, *ibid.* **12** (1973) 295.
3. M. ABKOWITZ and R. C. ENCK, *Phys. Rev.* **B25** (1982) 2567.
4. S. O. KASAP, "Handbook of Imaging Materials" (Dekker, New York, 1991) p. 329.
5. S. O. KASAP and C. JUHASZ, *J. Mater. Sci.* **21** (1986) 1329.
6. M. E. SCHARFE, "Electrophotography Principles and Optimization" (Wiley & Sons, 1984).
7. W. E. SPEAR, *Proc. R. Soc.* **A 420** (1968) 201.
8. G. PFISTER and H. SCHER, *Adv. Phys.* **27** (1978) 747.
9. J. M. MARSHALL, *Rep. Progr. Phys.* **46** (1983) 1235.
10. V. I. MIKLA, PhD Thesis, Odessa State University, 1984.
11. J. TAUC, "Amorphous and Liquid Semiconductors" (Plenum, New York, 1974) p. 159.
12. A. R. MELNYK, *J. Non-Cryst. Solids* **35/36** (1980) 837.
13. M. ABKOWITZ, F. JANSEN and A. R. MELNYK, *Phil. Mag.* **B51** (1985) 405.
14. M. ABKOWITZ and J. M. MARKOVICH, *Solid State Commun.* **44** (1982) 1431.
14. K. TANAKA, *Current Opinion in Solid State & Materials Science* **1** (1996) 567.
15. M. ABKOWITZ and F. JANSEN, *J. Non-Cryst. Solids* **59/60** (1983) 953.
16. J. SCHOTTMILLER, M. TABAK, G. LUCOVSKY and A. I. WARD, *ibid.* **4** (1970) 80.
17. N. F. MOTT and A. E. DAVIS, "Electronic Processes in Non-Crystalline Materials" (Clarendon Press, Oxford, 1979).
18. V. I. MIKLA, *Materials Science & Engineering* **B49** (1997) 123.
19. J. M. MARSHALL, F. D. FISHER and A. E. OWEN, *Phys. Stat. Solidi* **A25** (1974) 419.
20. P. J. WARTER, *Appl. Opt. Suppl.* **3** (1985) 65.
21. M. ABKOWITZ and R. C. ENCK, *Phys. Rev.* **B27** (1983) 7402.
22. M. KASTNER, D. ADLER and H. FRITZSCHE, *Phys. Rev. Lett.* **37** (1976) 1504.
23. B. POLISCHUK, S. O. KASAP, V. AIYAH and M. ABKOWITZ, *Can. J. Phys.* **69** (1991) 64.
24. S. M. VAEZI-NEJAD and C. JUHASZ, *J. Mater. Sci.* **23** (1988) 3286.
25. V. I. MIKLA, *J. Phys.: Condens. Matter.* **9** (1998) 9209.

Received 23 April 1999
and accepted 21 March 2000